Effect of solidification on a propagating dike

B. Taisne, S. Tait

HAL Id: insu-03606509
https://insu.hal.science/insu-03606509

Submitted on 11 Mar 2022

Effect of solidification on a propagating dike

B. Taisne[1] and S. Tait[2]

[1] Magma migration through the brittle crust from depth occurs by the propagation of hydraulic fractures or dikes. Volcanic eruptions occur at the last stage if and when a propagating dike reaches the surface. Dike propagation involves complex physics because of several processes that are simultaneously occurring such as viscous flow of magma, rock fracture, elastic deformation of the host rock, and potentially large changes of the physical properties of the magma (crystallization, degassing, solidification, etc.). Currently the most practical way in the field or in terms of field measurements to follow the migration of magma before it reaches the surface is the analysis of the seismicity generated; nevertheless, a physical model that quantitatively relates the flux of magma in the dike to the seismicity is lacking. We present here laboratory experiments involving propagation of a fluid-filled crack such that the fluid solidifies upon contact with the cold elastic host. We show that this can lead to a way of estimating the flux of the injection as a function of the surface creation rate. The latter is shown to be a more reliable gauge of magma flux than the upward propagating velocity. In the geologic application of a propagating dike, the rate of creation of surface area may be related to the rate of release of seismic energy. Although this latter relation needs further work to be quantitatively reliable, our new model nevertheless indicates how a new general framework can be constructed.

1. Introduction

[2] A crucial parameter determining the magnitude of a volcanic eruption is the flux of magma at the vent. The measurement of the flux is difficult even after an eruption begins, but there is currently no reliable method from precursory activity, such as seismic swarms, to estimate the flux of magma prior to its arrival at the surface. Such a method would be very useful because it would in principal give some advanced warning about the intensity of eruptive behavior. The idea behind the work described in this paper is to devise a way to use seismic events, caused by the migration of the magma at depth, as a precursory signal that can allow us to capture the physics of the injection before the onset of eruption. To interpret the field data in a clear albeit simplified framework, we propose analogue experiments to understand the temporal evolution of the dike as a function of the volumetric flux of injection.

[3] Solidification of the magma during propagation can be of primary importance. The fact that the magma can solidify during propagation implies a minimum value of the flux for a sustainable injection; if the flux is not high enough, the injection will freeze and stall at depth instead of reaching the surface [*Rubin*, 1993; *Bolchover and Lister*, 1999]. Furthermore, field analyses reveal geometrical discontinuities in dikes (such as dikes branching out or overlapping) and seismic analyses reveal discontinuities in the propagation highlighted by seismic bursts [*Hayashi and Morita*, 2003]. These field and seismic observations together suggest that the propagation of magmatic dikes in nature exhibits discontinuities. A question addressed here is whether such discontinuities are the result of heterogeneity in the surrounding medium or whether they are part and parcel of the process of propagation with solidification.

[4] We first demonstrate by analysis of our experimental data that one cannot straightforwardly extract useful information on the flux by simply trying to deduce the upward velocity of the fissure from accurate seismic locations, as has been done in a number of pioneering papers to follow propagating dikes. We show that a more reliable parameter is the temporal evolution of the surface area of the fissure, which can be related to the physical parameters that control the dike propagation such as rock and magma properties and most importantly the flux of the injection.

2. Experimental Approach

[5] The experiments described here are one step of complexity up from those used to study constant volume propagation [*Taisne and Tait*, 2009] or propagation with constant reservoir overpressure [*Menand and Tait*, 2002], which were both performed under isothermal conditions. The tank is made of Plexiglas with a square horizontal cross section of

[1]Équipe de Sismologie, Institut de Physique du Globe de Paris, Paris, France.
[2]Équipe de Dynamique des Fluides Géologiques, Institut de Physique du Globe de Paris, Paris, France.

30 × 30 cm and 50 cm high. Injection was achieved via a deformable (rubber) linear opening at the base of the tank. Just prior to injection, we remelted the gelatin close to the two walls of the tank parallel to the injection and replaced it with water [*Taisne and Tait*, 2009]. We added to the setup a temperature-controlled reservoir fixed at the bottom of the tank. Prior the beginning of the injection, we performed a 2 cm vertical precut using a mobile blade from the reservoir, which did not influence the experiment but acted to force the plane of propagation to be perpendicular to the visualization system, consisting of a digital camera taking a picture every 5 or 10 s. (Time can be conveniently changed during an experiment with a minimum of 1 s between two successive frames.) The experiments were performed at constant volumetric flux achieved by means of a "giant" syringe with a computer-controlled piston (the piston velocity and the volumetric flux are linearly related). In this paper we present two sets of experiments at constant flux of injection but with different thermal conditions. One set of experiments was performed under isothermal conditions to avoid any temperature changes that could affect the physical properties of the fluid, and the other set was performed under nonisothermal conditions with a paraffin wax. The gelatin temperature was beneath the wax solidus, which led to freezing of the wax during the injection process. The wax thus exhibited strong temperature-dependent rheology in the form of a well-characterized phase change under laboratory conditions (see Figure 3c). To control the initial temperature of the paraffin wax, a colloidal coil allowed the circulation of temperature-controlled water inside the reservoir. The temperature of the gelatin was controlled via the laboratory temperature (controlled by air conditioning). We used a pair of thermocouples to measure the temperature difference between the reservoir (paraffin wax) and the gelatin (analogous to the host rock). Typical values for the temperature of the gelatin were from 15°C to 20°C and the paraffin wax was injected at a temperature above the solidus of the paraffin (27°C) but not higher than 45°C.

[6] The thermal viability of a magma flow in an open conduit (i.e., neglecting fracturing effects) has been studied for some time [*Delaney and Pollard*, 1982; *Bruce and Huppert*, 1990; *Lister*, 1994a, 1994b; *Fialko and Rubin*, 1998]. In the case of hydrofracturing, *Lister and Kerr* [1991] proposed that the solidification, or a drastic change of the magma viscosity due to cooling, has an effect similar to that of an increased effective fracture toughness of the host rocks. *Rubin* [1993] and then *Bolchover and Lister* [1999] studied the competition between fracturing and solidification and they showed the existence of a threshold value under which solidification prevents propagation.

[7] In the work cited, key parameters are the temperature of the injected fluid (T_m), the temperature of the host rocks (T_∞), the temperature of the liquid phase change (T_s), and the volumetric flux of injection (Q). In this paper, we add the effect of fracturing with respect to these previous studies via the fracture toughness (K_c). We also take into account the effect of the buoyancy that results from the density difference between liquid and host rock ($\Delta\rho g$).

[8] To describe our experimental conditions, we derived two dimensionless parameters representing the thermal conditions (dimensionless temperature Θ) and the dynamical conditions (dimensionless flux Φ). The dimensionless

temperature Θ (equation (1)) is bounded between two extreme values, 0 when $T_m \gg T_s$ and 1 when $T_m \sim T_s$:

$$\Theta = \frac{T_s - T_\infty}{T_m - T_\infty}. \tag{1}$$

The dimensionless flux Φ could be defined in more than one way. We chose to derive it as a ratio of scales for heat flux advected into the fissure by flow and that lost by conduction to the gelatin host. If H, B, and L are characteristic dimensions for the fissure, H the thickness, B the horizontal breath, and L the length,

$$\Phi = Q\rho C_p \Delta T \frac{H}{\kappa \rho C_p \Delta T L B} = \frac{QH}{\kappa L B}, \tag{2}$$

where κ is the thermal diffusivity. If we apply the pressure balance arguments that are presented in section 3.1 (equations (5) and (6)) and use the standard relationship between elastic shear modulus (G) and Young's modulus (E) with Poisson's ratio $\nu = 0.5$, we obtain

$$\Phi = \frac{3Q\Delta\rho g}{2\kappa E} \tag{3}$$

as the definition for dimensionless flux.

3. Results

[9] Photographs taken regularly and perpendicular to the plane of the propagation allowed us to measure the length and width of the fissure as a function of time. In the case of experiments involving the solidification effect, we used the surface area occupied by the fissure as a function of time to characterize its propagation. To do so we developed an image analysis procedure which made use of the color contrast between fluid and gelatin to count automatically the number of pixels where the crack is present and convert it into an area.

3.1. Isothermal Experiments

[10] In these experiments, we studied the lengths of cracks as a function of time. After an initial phase of growth in both horizontal and vertical directions, the vertical propagation due to buoyancy became predominant and a constant vertical velocity was established (as shown by *Heimpel and Olson* [1994]). In some cases a subtle increase of velocity occurred close to the surface, which has been interpreted in terms of an interaction with the free surface boundary condition at the upper surface by *Rivalta et al.* [2005].

[11] We focus now on the mean upward propagation velocity and compare the experimental results with the prediction of a scaling law derived from pressure balances in the head region. This region can be identified from photographs (Figure 1). We can obtain an estimate of the velocity by dividing the volumetric input flux by the cross-sectional area of the crack in a horizontal plane, approximated as HB (where H and B correspond to the approximate thickness and the breadth, respectively):
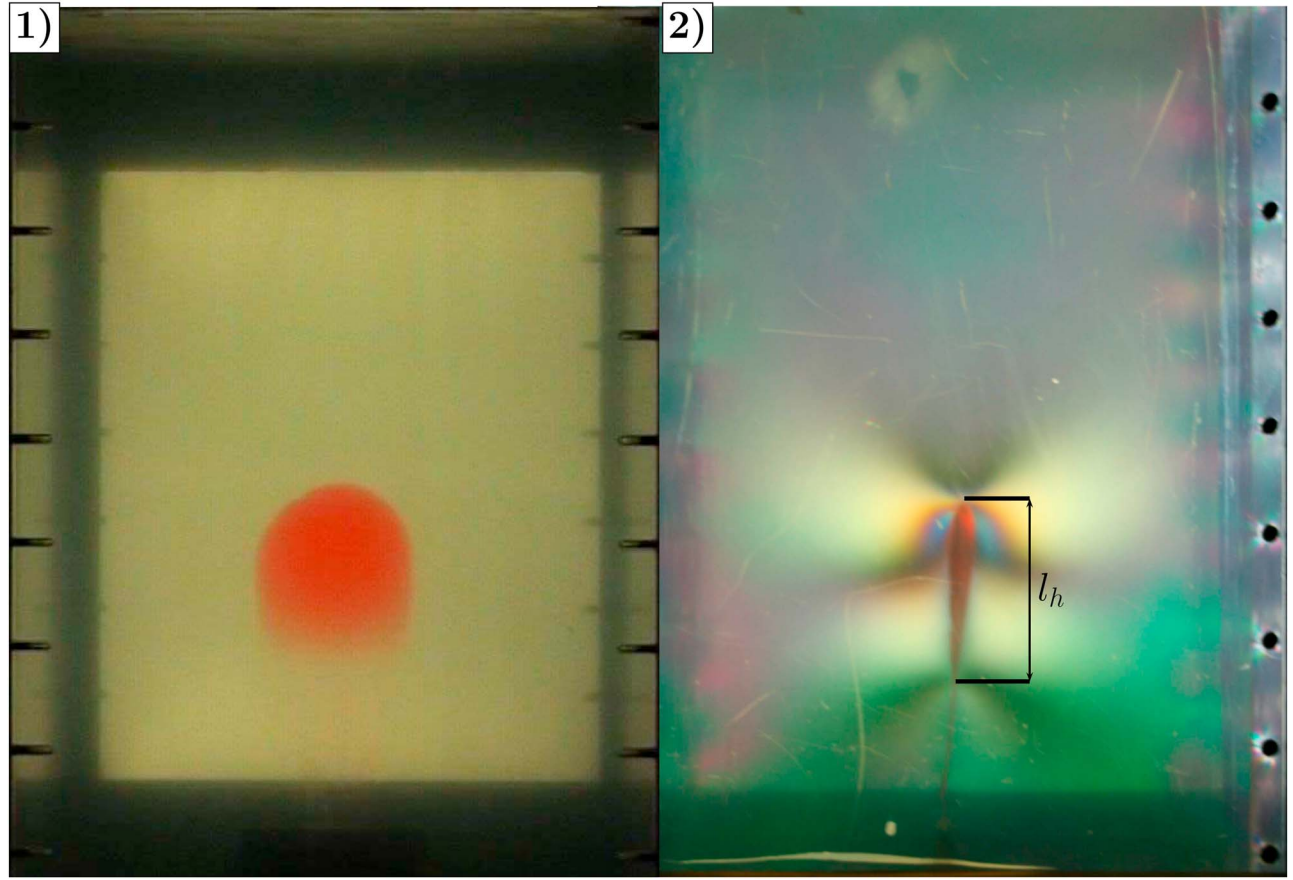
$$C \sim \frac{Q}{HB}. \tag{4}$$

Figure 1. Front and side view of an experiment involving constant flux of injection, and isothermal conditions (experiment 6, Table 1): (left) smooth boundary between the fluid and the elastic medium, and how the thicker head can be identified by its stronger color; (right) photoelastic fringes that help visualize the geometry and intensity of the stress field around the head region.

To obtain an estimate of HB, we consider the balance of forces in the head of the crack. We suppose that the length L and the width B are the same order of magnitude and that the buoyancy (P_b), the elastic pressure (P_e), and the fracturing pressure (P_f) are also of the same order of magnitude:

$$P_b \sim \Delta\rho g L \sim \Delta\rho g B,$$

$$P_e \sim \frac{G}{1-\nu}\frac{H}{B},$$

$$P_f \sim \frac{K_c}{\sqrt{B}}. \tag{5}$$

From $P_b \sim P_e$ in the set of equations (5), we obtain

$$HB \sim \Delta\rho g B^3 \frac{1-\nu}{G}. \tag{6}$$

Considering that $P_b \sim P_f$ (equation (5)) and combining with equation (6), equation (4) can be expressed as follows:

$$C \sim \frac{QG\Delta\rho g}{(1-\nu)K_c^2}. \tag{7}$$

[12] The comparison of the mean velocity, extracted from the isothermal experiments (Table 1), as a function of the scaling law, equation (7), is shown in Figure 2. Most points fall on the line. The two points that fall above the 1:1 line correspond to the lowest flux of injection for each of the two different fluids (experiments 4 and 6, respectively oil and heptane). As is the case in previously published work [e.g., *Heimpel and Olson*, 1994], we used different fluids to obtain varying amounts of buoyancy (see Table 1), some of which are hydrophobic (oils and heptane). The effect of the surface energy for experiments involving hydrophobic fluid

Table 1. Experimental Conditions for the Constant Flux Injection of an Isothermal Liquid[a]

	Q (m^3 s^{-1})	E (Pa)	$\Delta\rho$ (kg m^{-3})	μ (Pa s)	c (m s^{-1})	l_h (m)
1	7.35×10^{-6}	1224	330	4.0×10^{-4}	1.71×10^{-2}	1.00×10^{-1}
2	6.15×10^{-6}	1163	330	4.0×10^{-4}	1.61×10^{-2}	1.53×10^{-1}
3	2.01×10^{-6}	2600	335	4.0×10^{-4}	4.90×10^{-3}	1.37×10^{-1}
4	2.35×10^{-7}	3994	102	7.0×10^{-2}	3.32×10^{-4}	1.70×10^{-1}
5	1.41×10^{-6}	3994	102	7.0×10^{-2}	1.09×10^{-3}	1.70×10^{-1}
6	9.42×10^{-7}	1659	330	4.0×10^{-4}	5.76×10^{-3}	8.30×10^{-2}

[a]Heptane was used for experiments 1, 2, 3, and 6 and vegetal oil for experiments 4 and 5; c, mean value of the velocity, and l_h, head length.
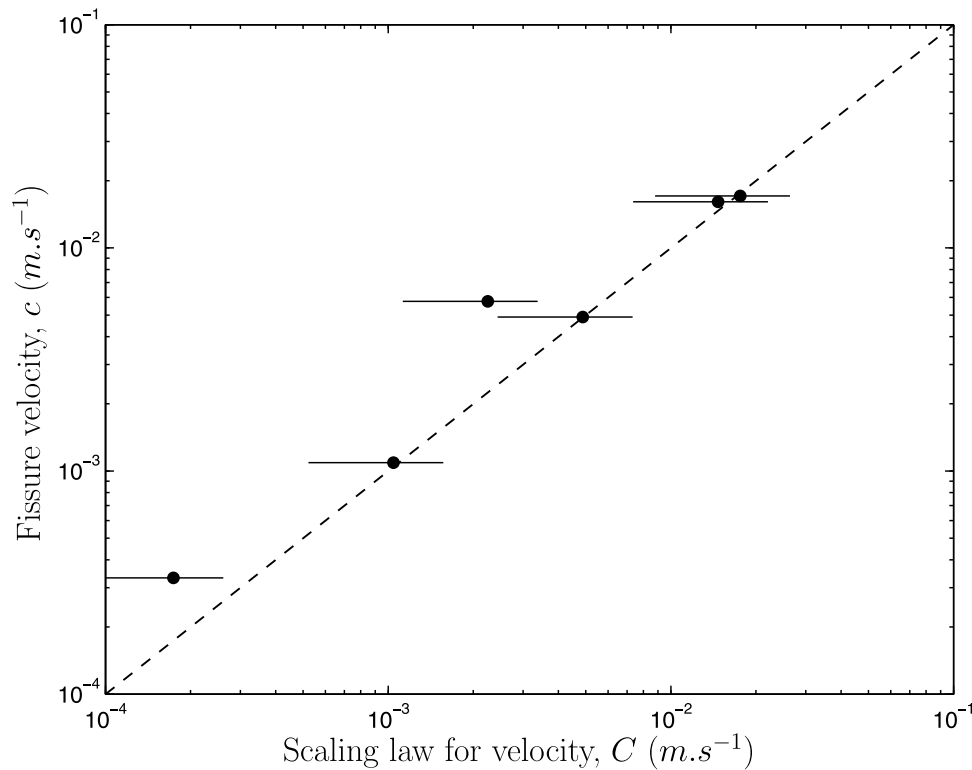
Figure 2. Vertical propagation velocity of the fissure as a function of the scaling law (equation (7)). See Table 1 for experimental conditions.

is discussed by *Taisne and Tait* [2009]. In the case of these two points in Figure 2, we surmise that the effect of the surface energy led to velocities measured in the experiments being a little higher than the prediction of equation (7), an effect that is not present for higher fluxes (continuity of the fluid from source to tip).

[13] We note the absence of the fluid viscosity in equation (7), which can be interpreted as reflecting a passive role of the tail compared to the head region. The tail can therefore be seen as a pathway for the fluid to migrate from the source to the head region which, under steady conditions, maintains a head of constant size and shape that is big enough to crack the host. The thickness of the tail is a function of the viscosity as well as the flux. From this relation we can, if desired, replace the flux in equation (7) by an expression containing the viscosity.

[14] The presence of the fracture toughness in expressions for the velocity (equation (7)) was noticed in previous experimental work [*Heimpel and Olson*, 1994; *Rivalta et al.*, 2005], whereas the role of this parameter was considered unimportant in the two-dimensional theoretical work of *Lister and Kerr* [1991].

3.2. Experiments Involving Solidification

[15] The typical morphology of fissures in this set of experiments is presented for illustration in Figure 3. The first observation that we made when observing the propagation of a fluid subject to solidification is the fact that the boundary between the fluid and the solid does not move continuously as in isothermal experiments. Propagation instead proceeds in a series of steps, in which the fissure grows, separated by periods in which the fissure swells due

to the input of fluid but does not grow in length or breadth. Figure 4 shows three contrasting experiments to illustrate this behavior. The values for parameters in these experiments are highlighted in Table 2. The second observation is that after a pause the propagation does not always initiate at the highest point of the fissure; it also initiates at the margins. Our understanding of the physical cause for the intermittent mode of propagation is that the solidification of the liquid at the margins affects the stress intensity factor that becomes smaller than the fracture toughness and, therefore, fracturing of the elastic medium is not possible. The swelling phase acts to increase the internal elastic pressure to the point where the stress intensity factor is high enough and overcomes the fracture toughness and propagation resumes. The fact that the propagation can be initiated at the margin instead of at the top of the fissure is not clear but is probably related to the local value of the stress intensity factor and therefore to the local geometry of the fissure margin.

[16] Even during propagation that, at first sight, appeared continuous, close visual observation revealed that propagation in fact occurred as a rapid succession of small steps (lasting for less than a second) that was hidden by the fact that the time between two pictures was greater than the time scale of two successive steps (because the time lapse between two successive frames cannot be less than 1 s because of the chosen apparatus).

[17] The graph of mean fissure velocity measured for each experiment, involving solidification effects, as a function of the scaling law derived for the isothermal case (equation (7)) shows that the law works poorly because virtually all calculated velocities fall beneath the line of proportionality (Figure 5). A better parameter turns out to be the surface
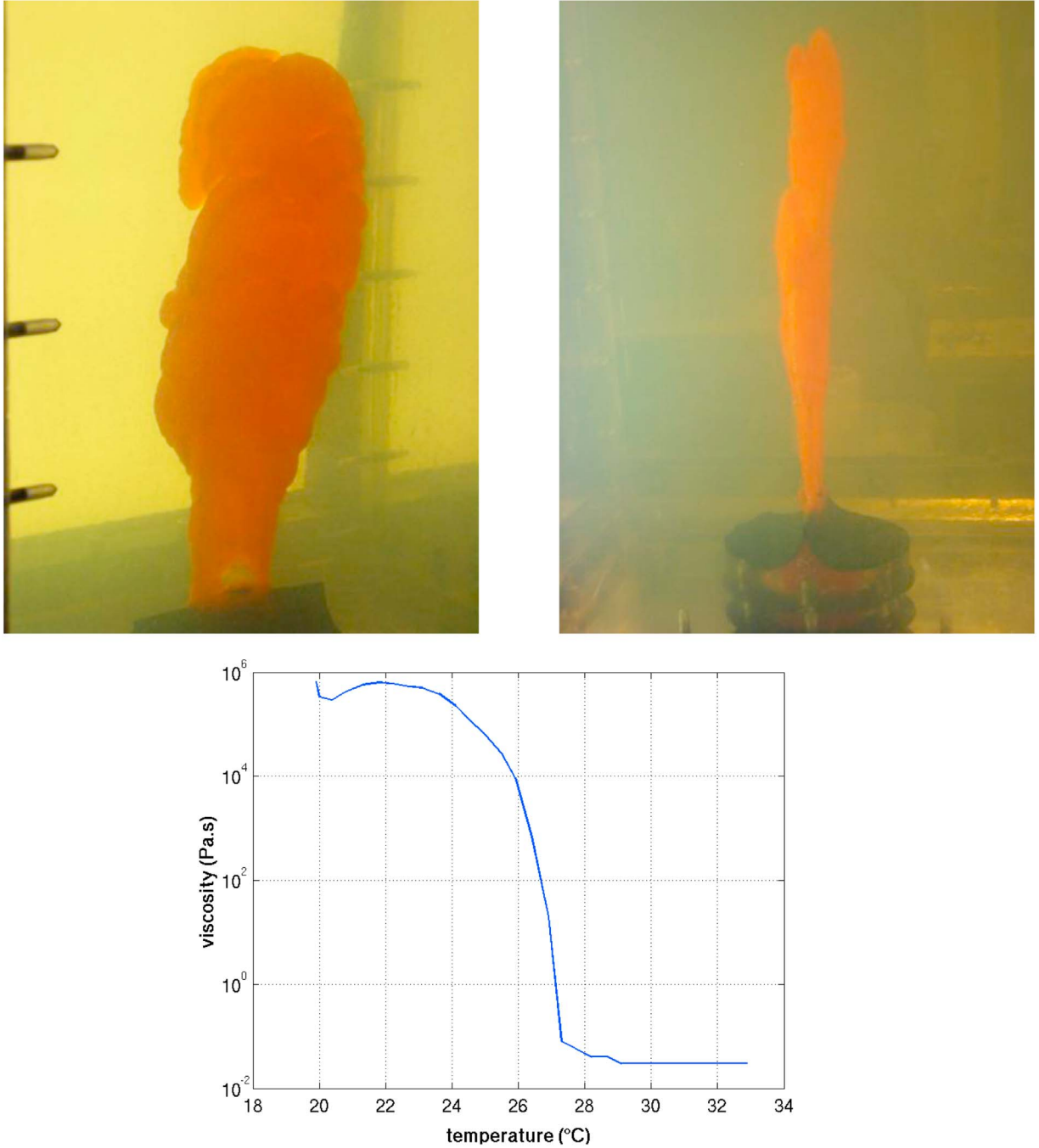
Figure 3. (top) Photographs showing discontinuities and irregularities observed due to the solidification effect; for scale, the injector is 10 cm in diameter. (bottom) Viscosity of the paraffin as a function of temperature; the temperature phase change can be identified at 27°C.

area (Σ) occupied by the fissure when viewed perpendicular to the plane of the fissure. A good approximation is to assume that the surface created during one step is proportional to the volume accumulated in the head between two steps; this leads to

$$Q\Delta t \sim \Delta\Sigma H, \tag{8}$$

where H still corresponds to the scale for the thickness. Between two steps, we observed a simultaneous lengthening

and thickening of the head region. This is consistent with the idea that the elastic pressure, which increases due to the thickening, was of the same order of magnitude as the buoyancy pressure, which also increased due to the lengthening:

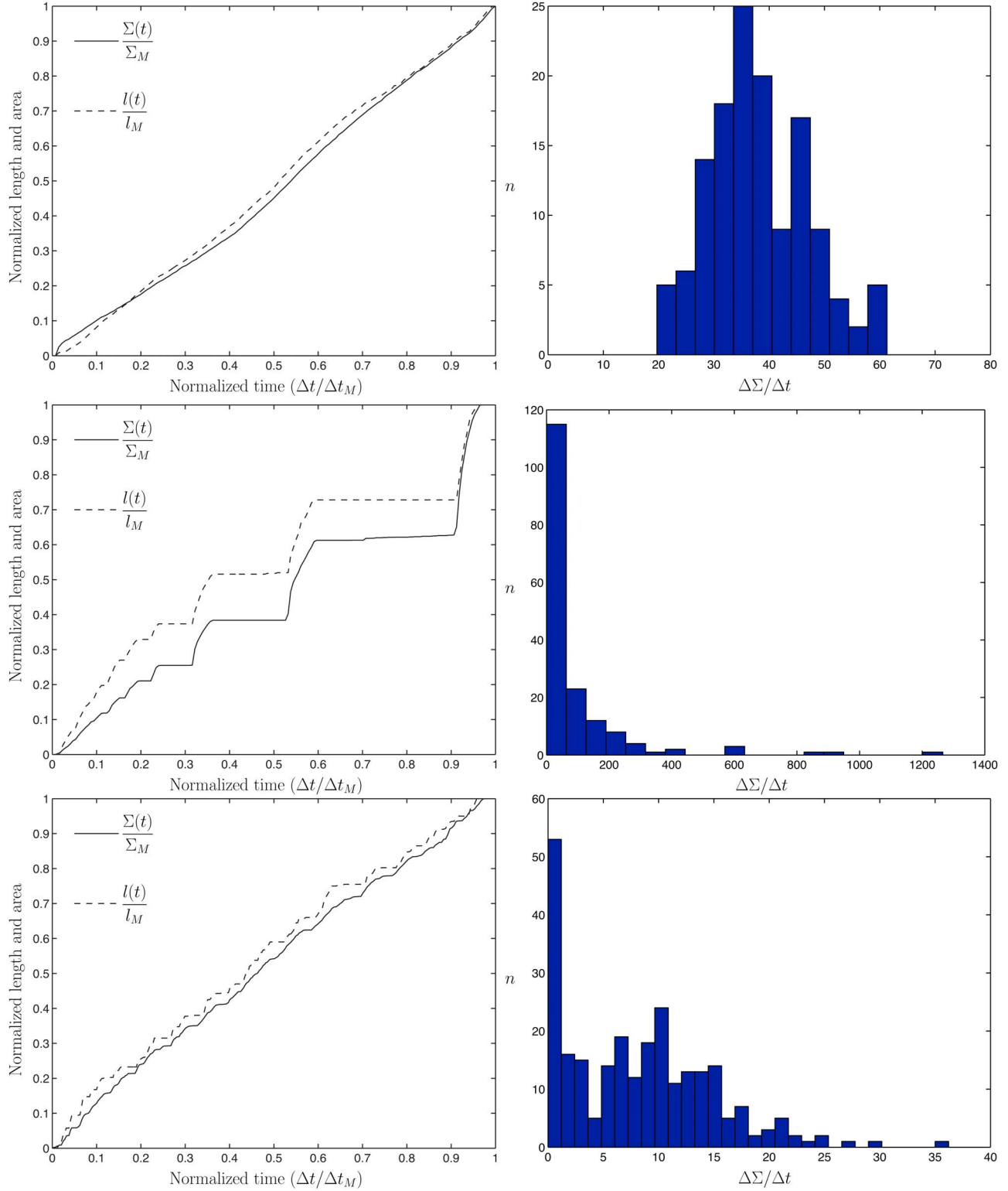$$\Delta\rho g L \sim \frac{G}{1-\nu}\frac{H}{L}. \tag{9}$$

Figure 4. (left) Temporal variation of length and surface area of the fissure; variables have been normalized by their final values to make them conveniently dimensionless so that both curves can be shown on the same graph. (right) Histogram of the surface creation rate during an experiment calculated by using each pair of successive images. From top to bottom, three kinds of behavior are illustrated: (top) a relatively continuous propagation (experiment 3, Table 2), (middle) a stepwise mode of propagation (experiment 11, Table 2), and (bottom) a combination of both kinds of propagation (experiment 16, Table 2).

Table 2. Experimental Conditions for the Constant Flux Injection of a Liquid Subject to Solidification[a]

	Q (m^3 s^{-1})	E (Pa)	T_m (°C)	T_∞ (°C)	Θ	Φ
1	1.3×10^{-7}	999	35.0	20.0	0.47	0.31
2	2.6×10^{-7}	1237	41.0	22.0	0.26	0.51
3[b]	2.4×10^{-8}	1039	48.7	22.0	0.19	0.06
4	9.9×10^{-8}	1039	48.7	22.0	0.19	0.23
5	4.5×10^{-8}	1810	32.5	24.0	0.35	0.06
6	6.3×10^{-8}	1810	32.5	24.0	0.35	0.08
7	3.31×10^{-6}	4753	30.4	16.0	0.77	1.68
8	6.3×10^{-7}	4829	31.0	16.0	0.73	0.35
9	5.5×10^{-7}	1661	29.5	17.0	0.80	0.80
10	1.05×10^{-6}	3947	33.0	17.0	0.62	0.64
11[b]	3.82×10^{-7}	3897	36.5	16.5	0.53	0.24
12	1.15×10^{-6}	5117	35.8	16.3	0.55	0.54
13	8.3×10^{-7}	1949	40.1	20.8	0.32	1.03
14	1.19×10^{-6}	5714	29.6	15.9	0.81	0.50
15	1.19×10^{-6}	5773	29.9	15.5	0.80	0.50
16[b]	1.22×10^{-6}	6189	41.5	16.1	0.43	0.48
17	9.79×10^{-7}	3186	52.8	18.8	0.27	0.74

[a]T_m, temperature of the liquid at the injecting point; T_∞, temperature of the elastic medium; Θ, dimensionless temperature of the system calculated at the injection point; Φ, dimensionless flux using $\Delta\rho = 230$ kg m^{-3} and $\kappa = 1.4 \times 10^{-6}$ m^2 s^{-1}.
[b]Experiments used as examples in Figures 4 and 8.

[18] If we assume that L is related to the buoyancy length (equation (5)) (see *Taisne and Tait* [2009] for further details), we can express H as follows:

$$H \sim \frac{(1 - \nu)K_c^{4/3}}{G(\Delta\rho g)^{1/3}}. \tag{10}$$

Combination of equation (10) and equation (8) yields a relation between the volumetric flux and the mean surface creation rate:

$$Q \sim \frac{\Delta\Sigma}{\Delta t} \frac{(1 - \nu)K_c^{4/3}}{G(\Delta\rho g)^{1/3}}. \tag{11}$$

[19] Figure 6 presents the mean surface creation rate calculated for each experiment as a function of the scaling law extracted from equation (11), and clearly the data are closer to this description than the one based on the velocity. For this kind of system (propagation of a fluid subject to solidification), the best variable to characterize fissure growth is therefore, in our view, the surface area of the crack and not its length (as suggested by Figure 6).

4. Time Evolution

[20] We now study more carefully the temporal evolution of the surface creation rate, instead of the mean surface creation rate. This provides more information on the physics of the injection (for example, effects related to thermal conditions) instead of just a quantitative estimation of the flux.

4.1. Representation of the Raw Data

[21] Comparing experiments 11 and 16 (Figure 4) it is not straightforward to estimate the relative durations of the phases of propagation compared with the phases of swelling. To better represent and quantify such differences, we plot the histogram of the surface creation rate between two
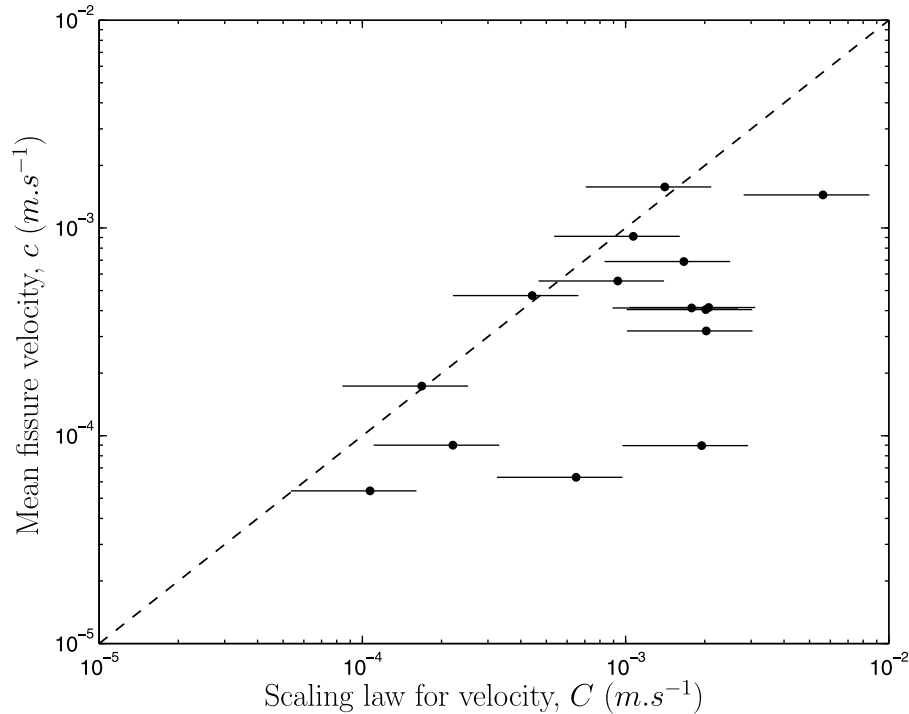

Figure 5. Mean fissure velocity measured for each experiment involving solidification effects as a function of the scaling law (equation (7)), derived for the isothermal case. The scaling law works poorly because virtually all calculated velocities are below the line of proportionality.
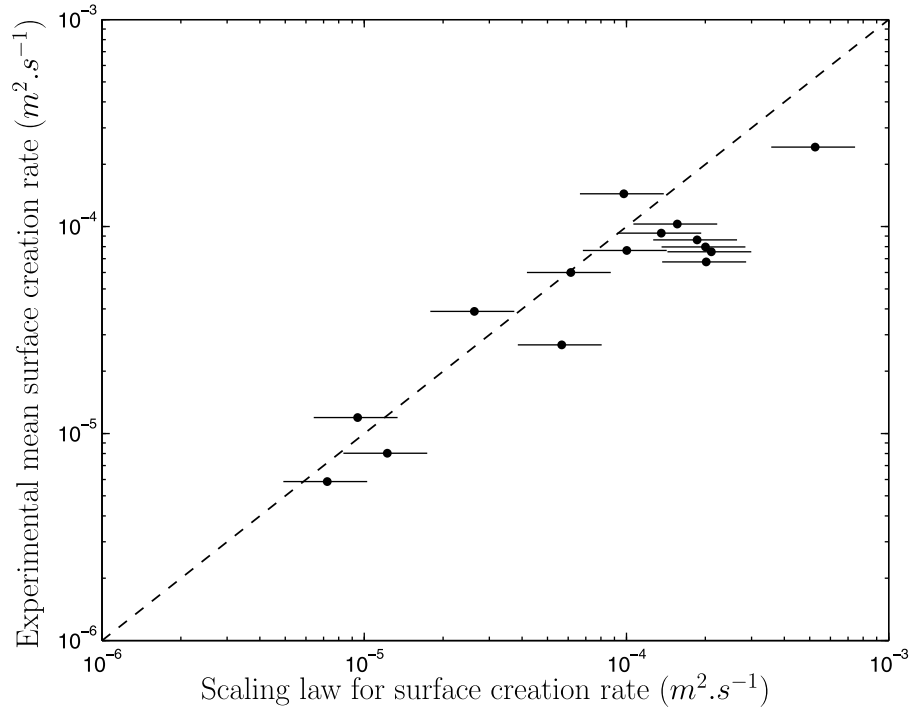
Figure 6. Experimental mean surface creation rate $\frac{\Sigma_M}{\Delta t_M}$, as a function of the scaling law, $\frac{Qm(\Delta\rho g)^{1/3}}{K_c^{4/3}}$, derived from equation (11).

successive pictures. This mode of representation reveals significant differences between cases according to the conditions of the experiments.

[22] In the case of almost continuous propagation (Figure 4, experiment 3), we obtained a histogram that clearly presents a dispersion around a mean value, suggesting a Gaussian distribution of the surface creation rate with μ_G as the mean value and (σ as the standard deviation:

$$n_{\text{continuous}} \sim \frac{1}{\sigma\sqrt{2\pi}} \exp\left(\frac{(\tau/\tau_M - \mu_G)^2}{2\sigma^2}\right). \quad (12)$$

[23] On the other hand, the strongly stepwise mode of propagation (Figure 4, experiment 11) gives a histogram that can be characterized by many values at or close to zero with a rapid falloff in frequency toward higher values, suggesting an exponential behavior defined by

$$n_{\text{stepwise}} \sim \lambda \exp\left(-\lambda \frac{\tau}{\tau_M}\right), \quad (13)$$

where λ is a free-fitting parameter.

[24] In the case of intermediate behavior (Figure 4, experiment 16), we obtain histograms that can be viewed as a combination of the continuous and the stepwise mode of propagation with a maximum at zero and a local secondary maximum, in this case around 10 mm^2 s^{-1}. To describe this intermediate behavior, we introduce a weighting coefficient, α, between equations (12) and (13) to obtain

$$n_{\text{intermediate}} \sim \alpha n_{\text{stepwise}} + (1 - \alpha)n_{\text{continuous}}. \quad (14)$$

Equations (12), (13), and (14), defined for the description of the experimental data, are shown in Figure 7.

4.2. Cumulative Curves

[25] To compare all experiments on the same plot, we normalize the surface creation rate by the maximum value obtained during each experiment (see equation (15)); the
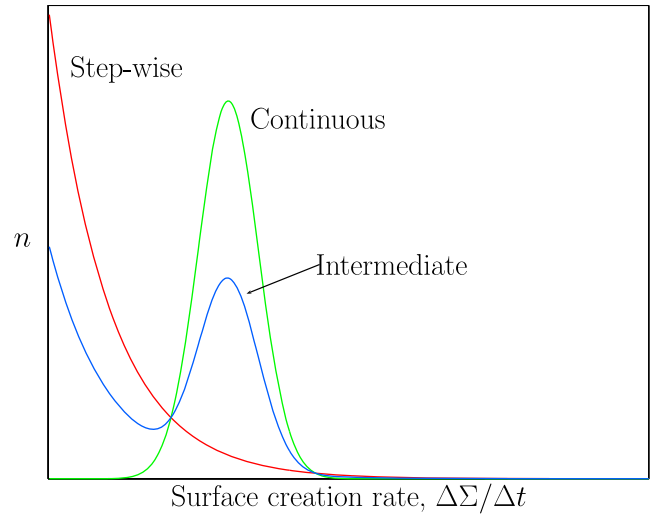

Figure 7. Simple description of the different modes of propagation. Continuous propagation (green curve) defined by equation (12), stepwise propagation (red curve) defined by equation (13), and intermediate propagation described by equation (14). Note the comparison with Figure 4 (left).
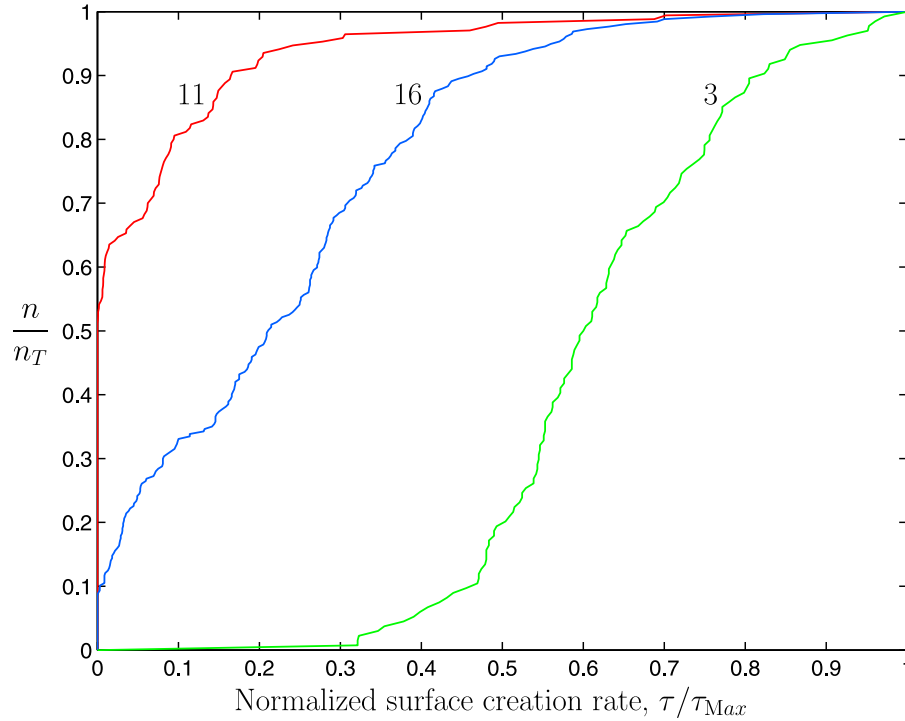
Figure 8. Cumulative curves corresponding to the histograms given in Figure 4. Numbers correspond to the individual experiments given in Table 2. Using this representation we are able to fit all the curves on the same graph.

parameter τ/τ_{max} is therefore included in the range [0; 1] for all the experiments:

$$\frac{\tau}{\tau_{max}} = \frac{\frac{\Delta\Sigma}{\Delta t}}{\frac{\Delta\Sigma}{\Delta t}\big|_{max}}. \tag{15}$$

We now use the cumulative curves of the normalized surface creation rate normalized by the total number of samples (pairs of pictures) available for each experiment (which depends on the total duration of the experiment and the time lapse between two successive pictures). This representation allows a direct comparison of all experiments on the same plot (Figure 8), which presents the data of Figure 4 (right). The cumulative curves corresponding to equation (14) can be characterized by four parameters [see equation (16) and Figure 9]:

$$\frac{n}{n_T} = \alpha\left(1 - \exp\left(-\lambda\frac{\tau}{\tau_M}\right)\right) + (1-\alpha)\frac{1}{2}\left(\text{erf}\left(\frac{\tau/\tau_M - \mu_G}{\sigma\sqrt{2}}\right)\right). \tag{16}$$

We accordingly use a combination of α, λ, μ_G, and σ to describe the data for each experiment by best fitting the data with equation (16), subject to the restrictions defined in Table 3.

[26] Among these four parameters, two are sensitive to the experimental conditions defined by the dimensionless temperature and the dimensionless flux: α, which can be seen as a proportion of values between the dike being halted and undergoing propagation, and μ_G, which corresponds to the

normalized mean surface creation rate during propagation events.

4.3.   The Parameters μ_G and α

[27] The two extreme values for μ_G and α are easily understandable. For strictly isothermal propagation, $\mu_G \to 1$ and $\alpha \to 0$. In the case of a pure stepwise propagation (that we can view as a limit of no propagation), we have $\mu_G \to 0$ and $\alpha \to 1$. We can link those extreme values with Θ and Φ by a simple reasoning (summarized in Table 4).

[28] For $\Theta \to 1$ (injection of a magma at its solidification temperature), we do not expect any propagation because of the dominance of cooling, which means $\mu_G \to 0$ and $\alpha \to 1$. In the opposite case, corresponding to the injection of a liquid at an infinite temperature ($\Theta \to 0$), we do not expect any effect of solidification and the behavior will tend to the isothermal case, $\mu_G \to 1$ and $\alpha \to 0$.

[29] Applying the same approach with the dimensionless flux, Φ, we find that, for $\Phi \to \infty$, the magma has no time to cool down and we have continuous propagation ($\mu_G \to 1$ and $\alpha \to 0$), and of course when $\Phi \to 0$ the magma cannot propagate ($\mu_G \to 0$ and $\alpha \to 1$).

[30] We now define two simple functions that present the same characteristic mathematical limits that we use to link the parameters of our experimental data to dimensionless governing parameters:

$$\mu_G = (1 - \Theta)^{\gamma_1}, \tag{17}$$
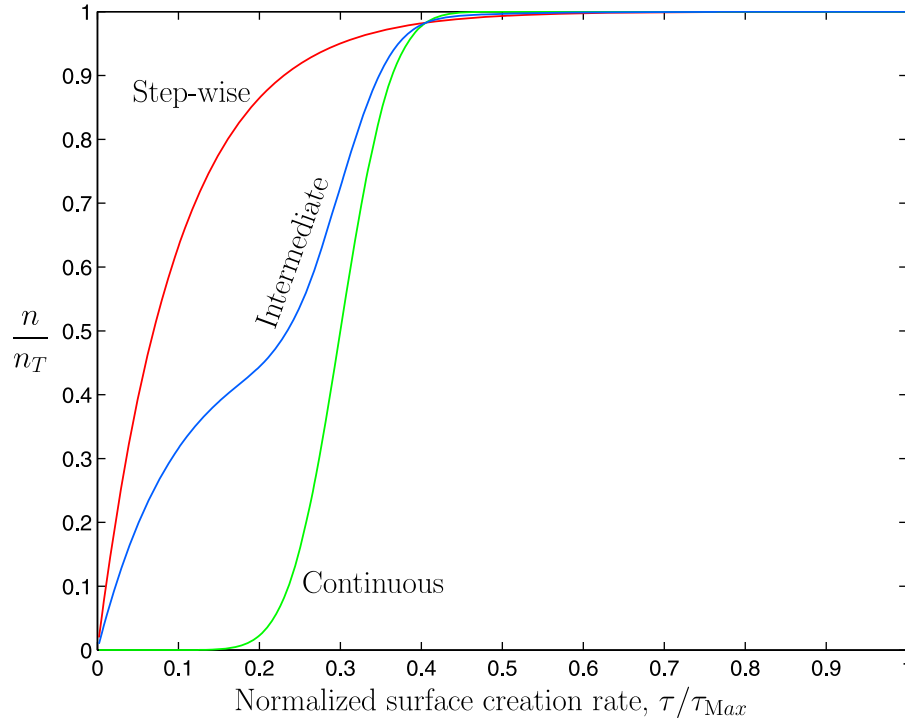
$$\alpha = \Theta^{\gamma_2}. \tag{18}$$

Figure 9. Cumulative curves corresponding to the description based on a combination of simple functions (equation (16)). Note the similarity with the cumulative curves extracted from the experiments (Figure 8).

For each experiment we determined γ_1 and γ_2. When plotting those values against Φ, we found that $\gamma_1 = \frac{0.824}{\Phi}$ and $\gamma_2 = 5.36\Phi$ (see Figure 10).

[31] Equations (17) and (18) can therefore be expressed using the experimental dimensionless parameters (Θ, Φ) as follows:

$$\mu_G = (1 - \Theta)^{0.824/\Phi} \qquad (19)$$

and

$$\alpha = \Theta^{5.36\Phi}. \qquad (20)$$

The position of Φ in the exponent is in accordance with the limit defined in Table 4. Figure 11 presents curves for different values of α and μ_G in the space (Θ, Φ).

5. Discussion

5.1. The Parameter Θ

[32] Note that, in Figure 11, for a given pair of (α, μ) there are two possible pairs of (Θ, Φ). For application to natural cases, the values of Φ are relatively unconstrained but we

can obtain a good idea of the value of Θ. Owing to the fact that the magma is most likely to be injected at a temperature close to its liquidus, the dimensionless parameter Θ should typically lie in the range 0.9 to 0.95 [*Delaney and Pollard*, 1982].

[33] The evolution of Θ as a function of the different temperatures involved (equation (1)) is presented in Figure 12. Reasonable assumptions are to suppose that the temperature of the surrounding medium (T_∞) cannot exceed the solidus of the magma and that the temperature of the magma (T_m) cannot be below the temperature of the solidus. Those limits correspond to the dashed line in Figure 12. In Figure 12 (left), the temperature of the magma is fixed and the curve shows the evolution of Θ as a function of the evolution of T_∞. As the temperature of the surrounding medium decreases toward the surface, the value of Θ will naturally tend to a value of 1. In Figure 12 (right), the temperature of the host rocks is fixed and the curve represents the influence of the temperature of the magma flowing within the dike. The farther the magma travels, one would expect its temperature to decrease, and this will drive the value of Θ toward 1.

Table 3. Range of Values Acceptable for the Description of Our Experiments

Parameter	Range
α	[0, 1]
λ	>0
μ_G	[0, 1]
σ	>0

Table 4. Conceptual Limits for α and μ_G Giving Their Required Behavior as a Function of Extreme Values for the Dimensionless Parameters Θ and Φ

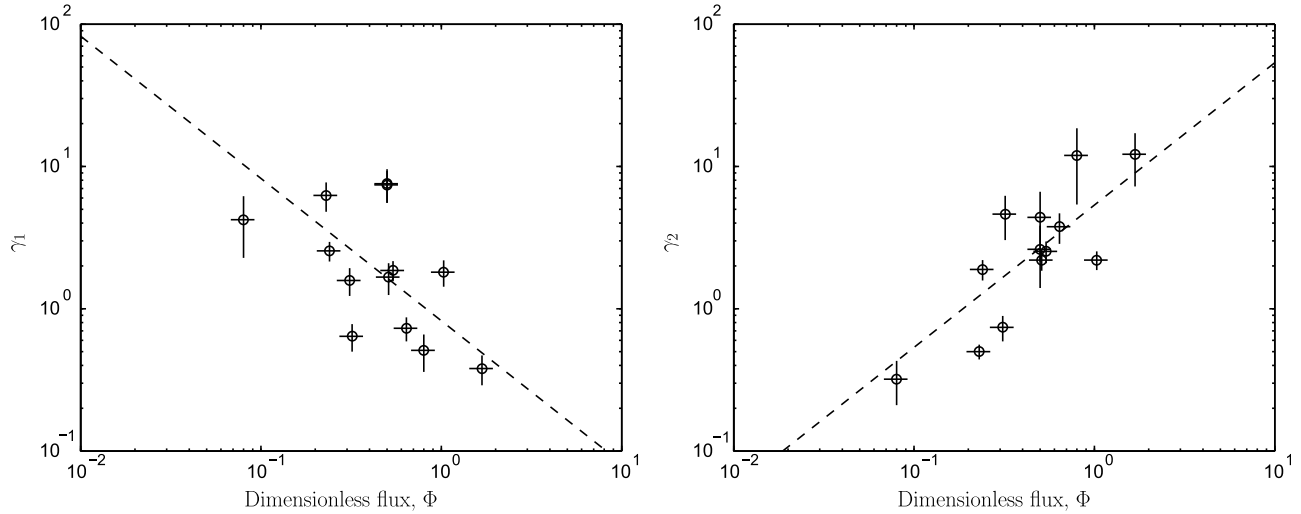|	Limits for α	Limits for μ_G
$\Theta \rightarrow 0$	$\alpha \rightarrow 0$	$\mu_G \rightarrow 1$
$\Theta \rightarrow 1$	$\alpha \rightarrow 1$	$\mu_G \rightarrow 0$
$\Phi \rightarrow 0$	$\alpha \rightarrow 1$	$\mu_G \rightarrow 0$
$\Phi \rightarrow \infty$	$\alpha \rightarrow 0$	$\mu_G \rightarrow 1$

Figure 10. (left) Representation of γ_1 as a function of Φ; dashed line represents $\gamma_1 = 0.824/\Phi$. (right) Representation of γ_2 as a function of Φ; dashed line represents $\gamma_1 = 5.36\Phi$.

[34] In the present paper we suppose that Θ is constant during the entire experiment (spatially and temporally). This is probably not the case because the temperature of the paraffin was controlled at the base of the experimental tank and must decrease from bottom to top. In other words, one can imagine a "local" value of Θ that varies as a function of distance from the source to the tip. This effect is probably dominant in the experiments starting with a relatively small value of Θ. The corresponding evolution corresponds to the Figure 12 (right) for T_∞ constant, and we see that a spatial variation of T_m implies a rapid increase in the value of Θ toward 1.

[35] The cooling of the paraffin close to the propagating tip of the fissure will have a strong effect on the style of propagation effectively observed and may drive a continuous propagation toward a stepwise mode of propagation.

5.2. Implications

[36] Our new experimental results, such as the morphology and the geometry of the fissure observed in some cases, show features that are compatible with geological observations.
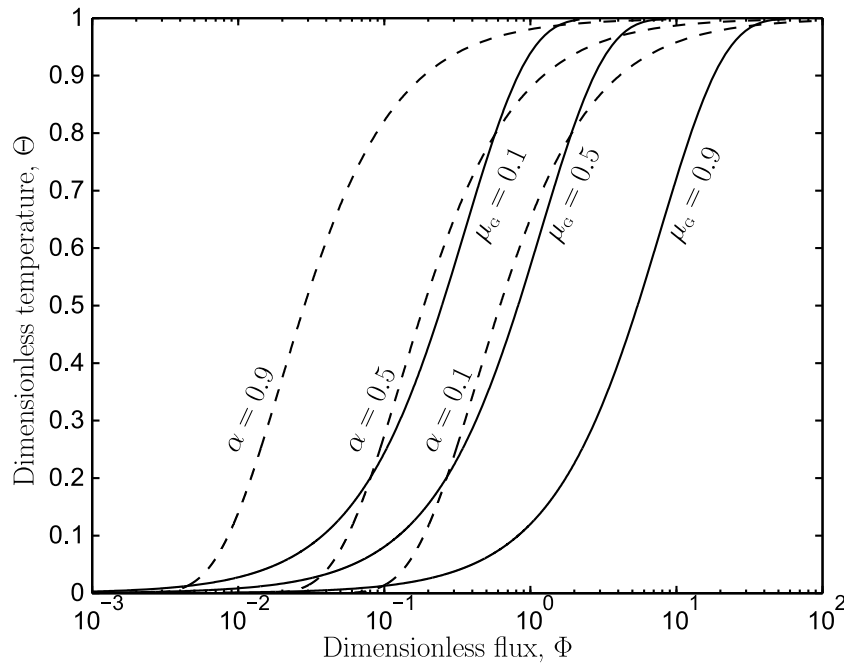

Figure 11. Dashed curves correspond to $\alpha = 0.1$, 0.5, and 0.9 (equation (20)). Solid curves correspond to $\mu_G = 0.1$, 0.5, and 0.9 (equation (19)). Note the two possible pairs of values of (Θ, Φ) for one pair of α and μ_G. From the reasonable constraint that the magma is most likely to be injected close to its liquidus temperature, we can exclude couples with the smallest value of Θ. For natural conditions, the value of parameter Θ, equation (1), is close to 1.
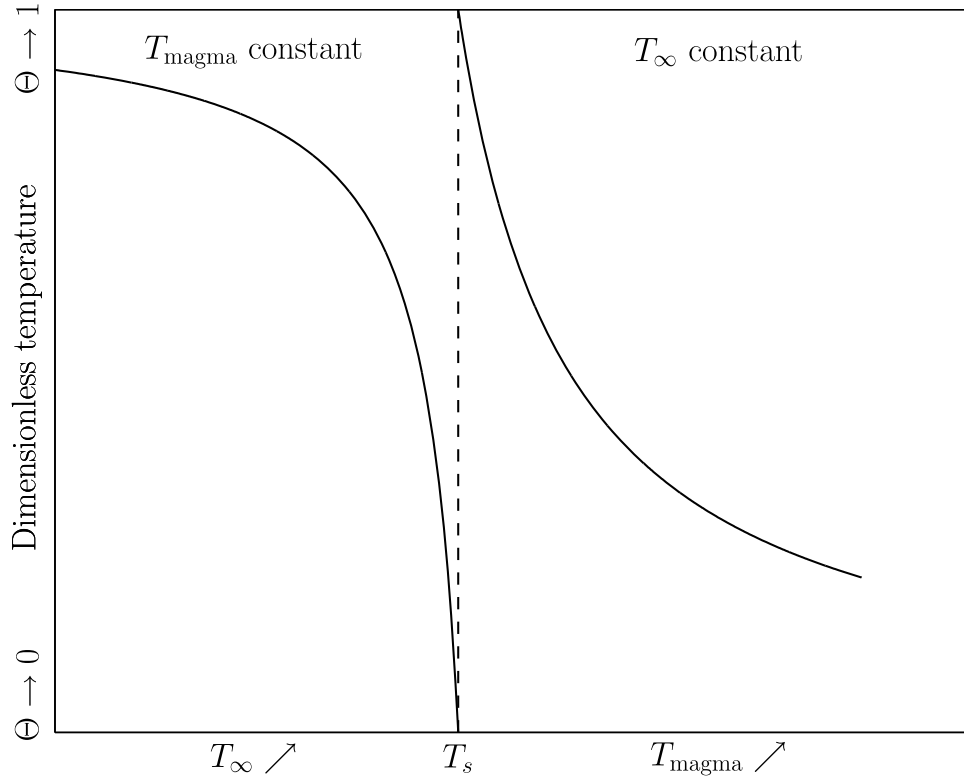
Figure 12. Variation of Θ (equation (1)) (left) as a function of an increasing temperature of the surrounding medium with a constant value for the magmatic temperature and (right) as a function of an increasing temperature of the liquid with a constant temperature of the surrounding medium. See text for more details.

The observation of overlapping dikes in some experiments may be applied to field observations made by looking at cross sections of dikes: it is not uncommon, for example, to observe offsets in such cross sections (sketches of field relations which give the impression of a jump). Such structures, however, result naturally from the mode of discontinuous propagation described here.

[37] We also suggest, by comparison with seismic data, that a new interpretation is possible regarding the bursts of seismic activity associated with the emplacement of a dike at depth. To explain such bursts or swarms of activity, there is no need to invoke intermittent input of magma from the source region (involving large variations in the flux at depth, which is not physically very plausible). Our work suggests that bursts are to be expected despite a constant input rate of magma from the source because the solidification that takes place can stop the propagation for a while, inducing deformation by swelling at constant area, until a new phase of propagation starts.

[38] To illustrate the potential of this idea to interpret natural data, we apply it to the crises recorded at Redoubt in 1989–1990 [*Power et al.*, 1994] and at Krafla in September 1977 [*Brandsdóttir and Einarsson*, 1979]. Because we cannot directly use the (unknown) surface creation rate as in our experimental analysis, we explore the following alternative. We assume that earthquakes represent perturbations of the ambient stresses related to the presence of the dike [*Rubin and Gillard*, 1998]. We then make an exactly similar analysis except that the input variable is the number of earthquakes per unit time, normalized by the maximum number of earthquakes per unit time, instead of the surface creation rate normalized by the maximum value of the surface creation rate. This analogy between surface creation rate and seismicity is preliminary and can probably be refined, but for the moment it seems a plausible way to proceed to illustrate the potential of this approach. Seismicity can also be produced when the dyke is swelling but not moving, but seismic bursts are more likely to be produced during propagation events. We obtained $\alpha = 0.515$ and $\mu_G = 0.226$ for the case of Redoubt and $\alpha = 0.079$ and $\mu_G = 0.839$ for the case of Krafla. Figure 13 represents those values in the space Θ, Φ defined from our experimental data. Using the fact that Θ is likely to be close to 1, only the upper part of the diagram is relevant for geological conditions. We can see, for example, that the dimensionless flux at Redoubt is quantitatively smaller than that at Krafla, which is consistent with the expected result for the flow as it moves toward the surface, given the large difference in magma viscosity. Although the analysis presented here is too preliminary to use for quantitative natural applications, we can nevertheless use the values of Φ that are deduced from this graph and the definition of Φ (equation (3)) to estimate the order of magnitude of fluxes. Assuming $E \sim 10^{10}$ Pa, $\Delta\rho \sim 100$ kg m^{-3}, and $\kappa \sim 10^{-6}$ m^2 s^{-1}, we obtain an estimate of ~ 10 m^3 s^{-1} for Reboubt and ~ 100 m^3 s^{-1} for Krafla. Those values should be treated with caution at this early stage, but they appear to be reasonable. We are currently pursuing this analysis in a more systematic way to
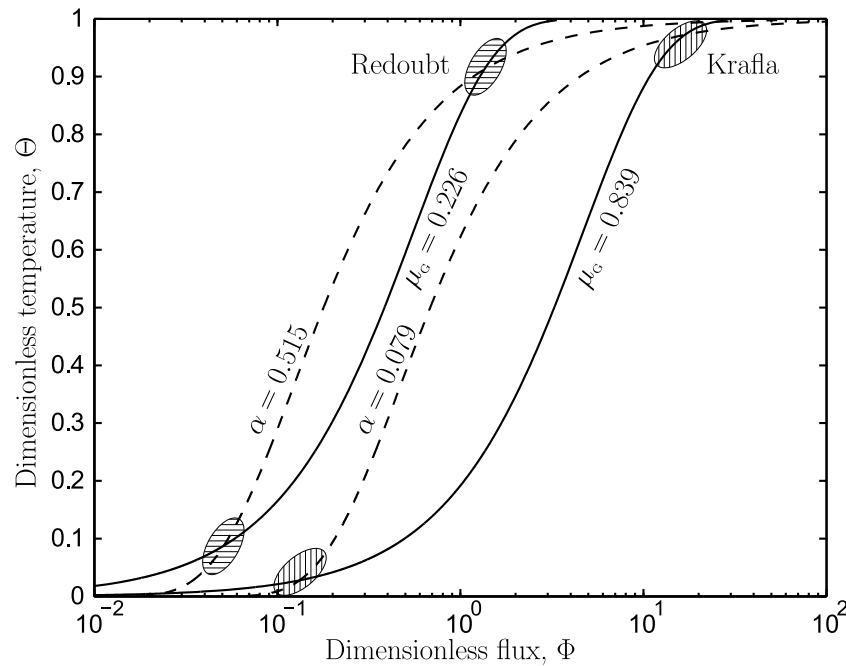
Figure 13. Representation of α and μ_G for the seismic crises recorded at Redoubt and Krafla. Horizontally and vertically hatched areas correspond to Redoubt and Krafla, respectively. See text for more details.

explore its potential to give information on propagating dykes before they reach the surface.

6. Conclusion

[39] We have shown here the importance of the solidification effect on the dynamics of dike propagation through cold crust, and in particular that this leads to a regime of intermittent propagation. Figure 14 presents a diagram that summarizes qualitatively the expected behavior of a propagating dike of magma under given dynamical and thermal conditions. The arrows present possible paths for both an increasing flux of injection (arrow 1) and successive
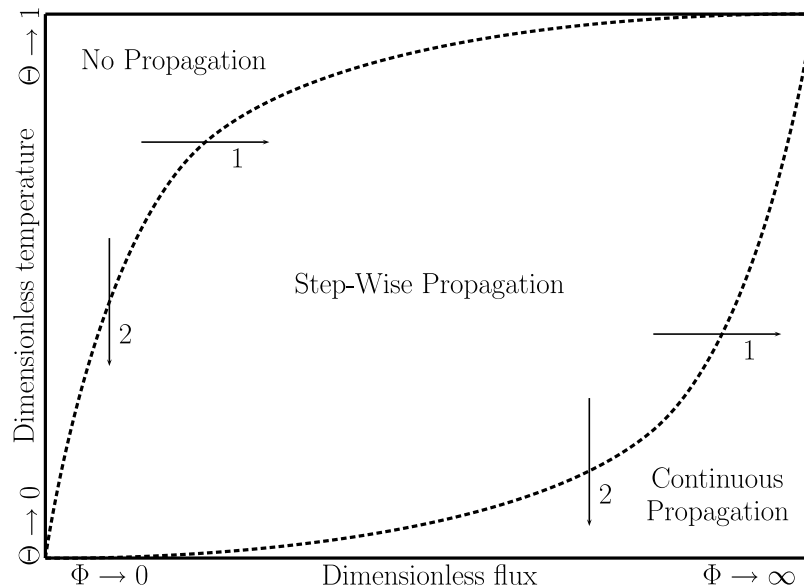

Figure 14. Diagram showing a qualitative representation of the different regimes of propagation as a function of dimensionless temperature (Θ) and dimensionless flux (Φ). Note that for a given dimensionless temperature a minimum value for the dimensionless flux is needed for propagation to occur (arrow 1, left). The path indicated by arrow 2 shows the effect of successive injections on the dimensionless temperature by increasing the temperature of the surrounding medium; this evolution can allow the system to cross the boundary between the two regimes. As $\Phi \rightarrow \infty$ and/or $\Theta \rightarrow 0$, propagation eventually becomes continuous.

injections that progressively warm up the surrounding medium (arrow 2). In both cases this can lead to a change in the mode of propagation.

[40] We have also proposed that successive bursts in seismicity can reflect the stepwise propagation of the magma at depth. In this case a link between the temporal and spatial distribution of such bursts can be related to the physical conditions of the injection such as the flux. Further development of these ideas will be presented in a future paper on the possible link between seismicity and physical properties of the injection.

References

Bolchover, P., and J. R. Lister (1999), The effect of solidification on fluid-driven fracture, with application to bladed dykes, *Proc. R. Soc. London, Ser. A*, *455*, 2389–2409.

Brandsdóttir, B., and P. Einarsson (1979), Seismic activity associated with the September 1977 deflation of the Krafla central volcano in north-eastern Iceland, *J. Volcanol. Geotherm. Res.*, *6*, 197–212.

Bruce, P. M., and H. E. Huppert (1990), Solidification and melting along dykes by the laminar flow of basaltic magma, in *Magma Transport and Storage*, edited by M. P. Ryan, chap. 6, pp. 87–101, John Wiley, Chichester, U. K.

Delaney, P. T., and D. D. Pollard (1982), Solidification of basaltic magma during flow in a dike, *Am. J. Sci.*, *282*, 856–885.

Fialko, Y. A., and A. M. Rubin (1998), Thermodynamics of lateral dike propagation: Implication for crustal accretion at slow spreading mid-ocean ridges, *J. Geophys. Res.*, *103*(B2), 2501–2514.

Hayashi, Y., and Y. Morita (2003), An image of magma intrusion process inferred from precise hypocentral migration of the earthquake swarm east of the Izu Peninsula, *Geophys. J. Int.*, *153*, 159–174.

Heimpel, M., and P. Olson (1994), Buoyancy-driven fracture and magma transport through the lithosphere: Models and experiments, in *Magmatic Systems*, *Int. Geophys. Ser.*, vol. 57, edited by M. P. Ryan, chap. 10, pp. 223–240, doi:10.1016/S0074-6142(09)60098-X, Academic, San Diego, Calif.

Lister, J. R. (1994a), The solidification of buoyancy-driven flow in a flexible-walled channel. Part 1. Constant-volume release, *J. Fluid Mech.*, *272*, 21–44.

Lister, J. R. (1994b), The solidification of buoyancy-driven flow in a flexible-walled channel. Part 2. Continual release, *J. Fluid Mech.*, *272*, 44–65.

Lister, J. R., and R. C. Kerr (1991), Fluid-mechanical models of crack propagation and their application to magma transport in dykes, *J. Geophys. Res.*, *96*(B6), 10,049–10,077.

Menand, T., and S. R. Tait (2002), The propagation of a buoyant liquid-filled fissure from a source under constant pressure: An experimental approach, *J. Geophys. Res.*, *107*(B11), 2306, doi:10.1029/2001JB000589.

Power, J. A., J. C. Lahr, R. A. Page, B. A. Chouet, C. D. Stephens, D. H. Harlow, T. L. Murray, and J. N. Davies (1994), Seismic evolution of the 1989–1990 eruption sequence of Redoubt Volcano, Alaska, *J. Volcanol. Geotherm. Res.*, *62*, 69–94.

Rivalta, E., M. Böttinger, and T. Dahm (2005), Buoyancy-driven fracture ascent: Experiments in layered gelatine, *J. Volcanol. Geotherm. Res.*, *144*, 273–285.

Rubin, A. M. (1993), On the thermal viability of dikes leaving magma chambers, *Geophys. Res. Lett.*, *20*(4), 257–260.

Rubin, A. M., and D. Gillard (1998), Dike-induced earthquakes: Theoretical considerations, *J. Geophys. Res.*, *103*(B5), 10,017–10,030.

Taisne, B., and S. Tait (2009), Eruption versus intrusion? Arrest of propagation of constant volume, buoyant, liquid-filled cracks in an elastic, brittle host, *J. Geophys. Res.*, *114*, B06202, doi:10.1029/2009JB006297.

B. Taisne, Équipe de Sismologie, Institut de Physique du Globe de Paris, Sorbonne Paris Cité, Univ Paris Diderot, UMR 7154 CNRS, F-75005 Paris, France. (taisne@ipgp.fr)

S. Tait, Équipe de Dynamique des Fluides Géologiques, Institut de Physique du Globe de Paris, Sorbonne Paris Cité, Univ Paris Diderot, UMR 7154 CNRS, F-75005 Paris, France.